RSC Advances



PAPER

View Article Online
View Journal | View Issue



Cite this: *RSC Adv.*, 2025, **15**, 16532

# Efficient and rapid removal of thiophene sulfides from fuel using zirconia-loaded phosphotungstic acid†

Rui Liang,[a] Yu Hu,[a] YuFang Ye[ab] and Qing Wang *[ab]

In this study, a new type of composite was synthesized *via* the sol–gel method. The structure and properties of the composite were analyzed using X-ray diffraction, scanning electron microscopy, nitrogen isothermal adsorption and desorption tests, Fourier transform infrared spectroscopy and X-ray photoelectron spectroscopy. Characterization results showed that phosphotungstic acid ($PW_{12}$) was successfully loaded on zirconium dioxide ($ZrO_2$). The oxidative desulfurization performance of 500 ppm dibenzothiophene (DBT) was studied with $H_2O_2$ as the oxidant and $x PW_{12}/ZrO_2$ as the catalyst. Under optimal conditions ($T$ = 60 °C, O/S = 2 and $m$ = 0.03 g), the desulfurization rate reached 97.85% within 20 min, and the activity did not decrease significantly after 8 cycles. The kinetics of the reaction was studied at different temperatures. Results showed that the oxidation rate conforms to quasi-first-order kinetics and the apparent activation energy is 23.32 kJ $mol^{-1}$. Therefore, the composite material is expected to be a catalyst for oxidative desulfurization.

Received 23rd March 2025
Accepted 29th April 2025

DOI: 10.1039/d5ra02041g

rsc.li/rsc-advances



## Introduction

With the development of society, the demand for cars as a means of transportation is increasing daily, resulting in an increase in the demand for fuel as a power source.[1] The sulfides in fuel oil mainly include thiophene, benzothiophene and alkyl substituted thiophene.[2] Their combustion releases a large number of sulfur dioxide and sulfate particles into the environment, which is the main cause of air pollution.[3] Long-term exposure to these pollutants poses a serious threat to human health.[4] Thus, to achieve the goal of green development, various countries around the world have formulated mandatory standards to ensure the quality of oil products and strictly control the sulfur content in fuel.[5–7] Therefore, ultra-deep desulfurization is applied to remove thiophene compounds containing aromatic structures, such as BT, DBT and 4,6-DMDBT; owing to the electronic effect of lone pair electrons and the steric hindrance effect of substituents, such aromatic structure sulfides are usually more difficult to remove.[8–11] Therefore, to effectively solve this problem and improve catalytic performance, catalysts with high activity need to be applied in the oxidation desulfurization system.

At present, fuel oil desulfurization methods are mainly divided into hydrodesulfurization[12] and non-hydrodesulfurization.[13] Hydrodesulfurization (HDS) is a desulfurization method that uses appropriate catalysts to convert sulfur-containing compounds into hydrogen sulfide and hydrocarbons. However, strict reaction conditions are required and equipment investment is huge. This limitation restricts its application in the field of fuel desulfurization. Thus, to overcome the shortcomings of HDS, non-hydrodesulfurization technology has been explored to achieve deep desulfurization. The main non-hydrodesulfurization methods include adsorption desulfurization,[14] biological desulfurization,[15] extraction desulfurization[16] and oxidation desulfurization.[17] Among them, oxidative desulfurization has become popular owing to its cost-effectiveness, straightforward operation and ability to achieve deep desulfurization under mild conditions.[18–22] This method involves the oxidation of organic sulfur compounds into sulfones or sulfoxides, followed by liquid-phase extraction using appropriate polar solvents.[23] The success of oxidative desulfurization depends on the selection of catalysts and oxidants. Hydrogen peroxide ($H_2O_2$), favored for its affordability and eco-friendliness, is a commonly utilized oxidant in oxidative desulfurization processes.[24–28] Nonetheless, catalysts are invariably required to enhance the efficiency of these desulfurization techniques. ODS can also be carried out in the presence of only oxidants, but it usually has extremely low desulfurization efficiency and needs to be conducted under rather harsh conditions. In ODS, catalysts play a very important role and can greatly enhance the desulfurization efficiency of ODS.

In recent years, polyoxometalate-derived heterogeneous catalysts have demonstrated remarkable activity in oxidative

[a]College of Chemistry and Chemical Engineering, Xinjiang Normal University, 830054 Urumqi, China. E-mail: wangqing@xjnu.edu.cn
[b]Xinjiang Key Laboratory of Energy Storage and Photoelecrocatalytic Materials, China

† Electronic supplementary information (ESI) available. See DOI: https://doi.org/10.1039/d5ra02041g

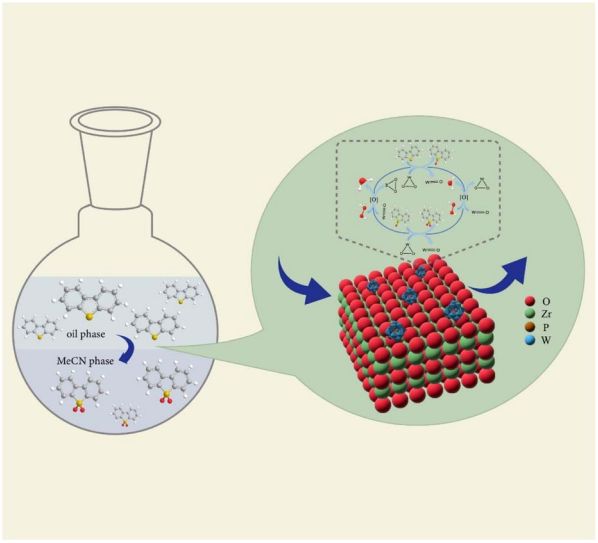


Scheme 1 Schematic mechanism of $x$PW$_{12}$/ZrO$_2$ in the process of oxidative desulphurization.

desulfurization, which is attributed to their substantial surface area and ease of separation from the reaction mixture. Studies indicate that when POM is supported on a strongly alkaline, weakly acidic, or neutral substrate, its chemical stability is compromised, leading to its leaching in polar solvents.[29,30] Building on previous investigations,[31] this study employed a metal oxide ($ZrO_2$) as a carrier for POM, utilizing the straightforward sol–gel technique to prepare $PW_{12}$ impregnated on zirconia, where acetonitrile was chosen as the extraction solvent and hydrogen peroxide served as the oxidizing agent for the oxidative desulfurization process (Scheme 1).

In this study, a novel recyclable heterogeneous catalyst ($x$PW$_{12}$/ZrO$_2$) was synthesized and characterized, and subsequently applied to the ODS process. By combining the advantages of $ZrO_2$ with the performance of $PW_{12}$, the performance of ODS was improved, and problems such as long reaction time, high catalyst consumption and easy leaching of the active species were overcome. Taking the model oil containing dibenzothiophene as the research object, the reaction conditions such as reaction temperature, catalyst dosage, reaction time and oxidant dosage were optimized. Next, under the optimal conditions, the performance of the catalyst was evaluated using other aromatic sulfur compounds such as benzothiophene and 4,6-dimethyldibenzothiophene. Finally, the kinetics and reaction mechanism in the oxidation desulfurization process were discussed.

## Materials and methods

### Materials and instruments

*N*-Butanol zirconium ($ZrO_4C_{16}H_{36}$) was purchased from Shanghai Maclin Biochemical Technology Co., Ltd (Shanghai, China). HCl was purchased from Tianjin Yongsheng Fine Chemical Co., Ltd Phosphotungstic acid ($H_3PW_{13}O_{40}\cdot xH_2O$) was purchased from Tianjin Guangfu Fine Chemical Co., Ltd (Tianjin, China). Acetonitrile and ethanol were purchased from Tianjin Zhiyuan Chemical Reagent Co., Ltd (Tianjin, China). Benzothiophene (BT), dibenzothiophene, and 4,6-dimethyldibenzothiophene (4,6-DMDBT) were purchased from Aladdin Biochemical Technology Co., Ltd (Shanghai, China). All reagents were at least analytical grade.

### Catalyst preparation

The preparation of $PW_{12}/ZrO_2$ was conducted following a literature method.[32] Initially, 10.0 mL of ethanol was added to 6.0 mL of *n*-butanol zirconium solution and stirred at 60 °C for 4 h. Once cooled to ambient temperature, the pH was adjusted to 2, and a mixture of ethanol, deionized water, and the requisite amount of phosphotungstic acid (0.06–0.84 mmol) was introduced, with continuous stirring at room temperature until a gel formed. The reaction was carried out at 180 °C for 12 h, after which it was allowed to cool to room temperature. The resulting product was thoroughly washed with deionized water, and subsequently dried at 100 °C. The resulting material was denoted as $x$PW$_{12}$/ZrO$_2$, where $x$ represents the loading amount of $PW_{12}$ corresponding to the added quantity. Based on the ICP-AES analysis, the actual loading capacities of $PW_{12}$ were determined to be 8.93 wt%, 14.62 wt%, 24.01 wt%, 36.80 wt%, and 44.89 wt%, respectively.

### Characterization

Scanning electron microscopy measurements were carried out using a ZEISS Sigma 300 (SEM; Oberkochen, German). Fourier transform infrared spectra were recorded on a Tensor 27 FTIR spectrometer (Bruker, Billerica, USA). The crystalline structures of the products were characterized using a DX-2800 X-ray diffractometer (XRD; Dandong Hao Yuan Instrument Co., Ltd, Dandong City, China). The specific surface area and pore size of the material were tested using a Mike ASAP2460 fully automatic specific surface area and pore analyzer (BET; USA). Gas chromatography-mass spectrometry was performed using 7890A-5975C (Agilent, USA). X-ray photoelectron spectroscopy was performed using a Thermo Kalpha (XPS; Thermo Fisher Scientific, USA).

### ODS experimental

DBT was dissolved in 100 mL of *n*-octane to obtain 500 ppm of model oil. In the process of oxidative desulfurization, when the temperature reached the specified temperature, the model oil (20 mL), acetonitrile (20 mL), catalyst (30 mg) and hydrogen peroxide were put into a two-neck flask and stirred at a certain stirring speed to start the oxidative desulfurization reaction. Samples were taken at regular intervals, tested by a fully automatic sulfur and nitrogen analyzer (JF-TSN-3000). Eqn (1) was used to calculate the DBT desulfurization rate ($S_R$), where $C_t$ is the sulfur concentration when the reaction proceeds for a certain long time and $C_0$ is the initial concentration of sulfur.

$$S_R = \frac{C_0 - C_t}{C_0} \times 100\% \quad (1)$$

## Results and discussion

### Catalyst characterization

The X-ray diffraction (XRD) patterns for $PW_{12}$, $ZrO_2$ and the $x$PW$_{12}$/ZrO$_2$ composite are depicted in Fig. 1. In the pattern of pure $ZrO_2$, the peaks located at the 2$\theta$ values of 24.12°, 28.07°, 31.28°, 34.18°, 35.3°, 41.18°, 49.81° and 55.33° belong to the (110), (011), (111), (200), (002), (−112), (022) and (310) crystal planes, respectively (PDF#37-1484). Upon loading $PW_{12}$ onto $ZrO_2$, the XRD pattern exclusively displayed the characteristic peaks of $ZrO_2$, suggesting that $PW_{12}$ is well-dispersed and uniformly distributed within the porous structure of the carrier. With an increase in the amount of $PW_{12}$, the diffraction peaks of the catalyst showed a changing trend from sharp peaks to wide peaks, indicating an increase in amorphous structure. This change might be due to the presence of excessive $PW_{12}$ in the synthesized catalyst, which hinders the crystalline growth of larger $ZrO_2$ nanoparticles and leads to the formation of a large number of amorphous structures.[33,34] Among the basic characteristics of materials, there are two morphology groups, consisting of crystalline and amorphous types. It should be noted that crystalline structures have sharp peaks, while amorphous structures have broader peaks in their XRD patterns. The calculation of crystal size based on the XRD pattern is possible and meaningful only for crystalline structures, and amorphous materials cannot be placed in this category for crystal size calculation.[35]

The morphologies of $ZrO_2$ and the $x$PW$_{12}$/ZrO$_2$ composite were examined using scanning electron microscopy (SEM). Fig. S1† illustrates the zirconia crystallites, which exhibit a well-defined tetragonal, short columnar structure.[36,37] As the concentration of $PW_{12}$ increased, aggregation phenomena and intermolecular accumulation of $PW_{12}$ molecules became increasingly evident. The presence of particles adhering to the $ZrO_2$ surface suggests the successful loading of $PW_{12}$ onto the $ZrO_2$ support. To further ascertain the distribution of $PW_{12}$ across zirconium dioxide, elemental mapping of the 36.80PW$_{12}$/ZrO$_2$ composite was conducted, as depicted in Fig. 2g–k. The energy-dispersive X-ray (EDX) elemental mapping images confirm the presence of Zr, P, W, and O elements within the composite material, indicating that $PW_{12}$ is uniformly dispersed on the surface of $ZrO_2$. At the same time, the main elements present in the sample are also confirmed in Fig. l. Table S1† shows the contents of Zr and W in EDX.

Fig. 3 presents the FT-IR spectra of $ZrO_2$ and the $x$PW$_{12}$/ZrO$_2$ composites. The $ZrO_2$ spectrum exhibits characteristic absorption bands at 3391 cm$^{-1}$, corresponding to the O–H stretching vibration of the surface Zr–OH groups, and at 1624 cm$^{-1}$, attributed to the vibrational modes of adsorbed water molecules and hydroxyl groups in Zr–OH. The three distinct peaks observed at 737, 588, and 491 cm$^{-1}$ are assigned to the Zr–O bond vibrations. In the spectrum of the composite, two new characteristic peaks emerge at 1038 cm$^{-1}$ (P–O) and 951 cm$^{-1}$ (W=O), confirming the successful incorporation of $PW_{12}$. Notably, when the $PW_{12}$ loading reached 36.80 wt%, significant spectral changes were observed, where certain $ZrO_2$ characteristic bonds exhibited reduced intensity or completely disappear, and the P–O and W=O bond intensities showed a marked enhancement.[31] These observations suggest strong interfacial interactions between $PW_{12}$ and $ZrO_2$. However,

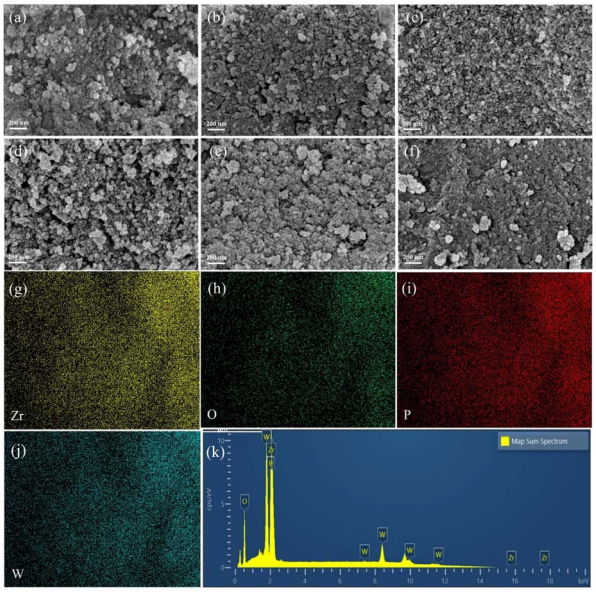


Fig. 2 SEM image of (a) $ZrO_2$, (b–f) $x$PW$_{12}$/ZrO$_2$ (8.93–44.89), and (g–j) corresponding elemental mapping of Zr, O, P, and W on 36.80PW$_{12}$/ZrO$_2$. (k) EDX image of 36.80PW$_{12}$/ZrO$_2$.

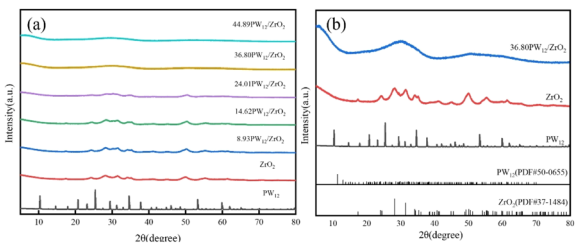


Fig. 1 XRD patterns of $PW_{12}$, $ZrO_2$ and $x$PW$_{12}$/ZrO$_2$ (8.93–44.89).

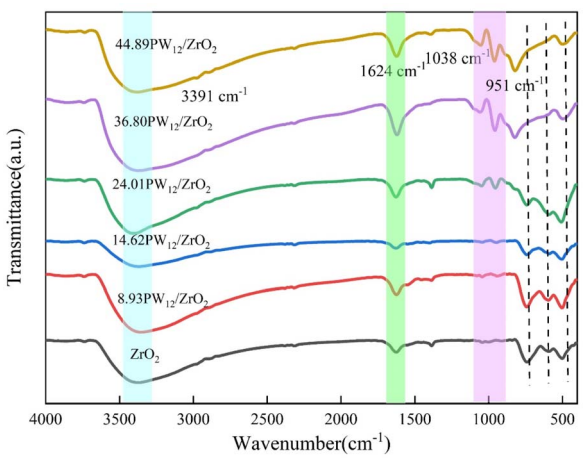


Fig. 3 FT-IR spectra of $ZrO_2$ and $x$PW$_{12}$/ZrO$_2$ (8.93–44.89).

a further increase in the $PW_{12}$ loading beyond 36.80 wt% did not result in additional enhancement in the P–O and W=O bond intensities, indicating the onset of $PW_{12}$ molecular aggregation or accumulation at higher loadings. This aggregation phenomenon likely limited a further increase in characteristic peak intensities due to molecular crowding effects. Thus, the systematic evolution of the FT-IR spectral features provides compelling evidence for the successful loading of $PW_{12}$ on the $ZrO_2$ support.

The nitrogen adsorption–desorption isotherms for $ZrO_2$ and the 36.80$PW_{12}$/$ZrO_2$ catalyst are presented in Fig. 4. It is evident that $ZrO_2$ exhibits a characteristic Type IV isotherm, accompanied by an H1 type hysteresis loop, indicating its mesoporous structure. This observation is consistent with literature reports.[38,39] In comparison to the pristine $ZrO_2$, the 36.80$PW_{12}$/$ZrO_2$ catalyst retained its mesoporous structure. However, the introduction of $PW_{12}$ led to a reduction in the specific surface area due to partial blockage of the pores within the $ZrO_2$ framework. As detailed in Table S2,† the pore size and pore volume of the 36.80$PW_{12}$/$ZrO_2$ catalyst increased from 3.16 nm to 6.11 nm and from 0.24 $cm^3\ g^{-1}$ to 0.27 $cm^3\ g^{-1}$, respectively. This enhanced structural configuration of the catalyst was instrumental in boosting its desulfurization performance, given that the larger pore size and volume facilitate better accessibility and diffusion of reactants and products within its porous network.

X-ray photoelectron spectroscopy (XPS) analysis was conducted to investigate the oxidation states and chemical composition of the 36.80$PW_{12}$/$ZrO_2$ nanocomposite. The full-scan XPS spectrum, as depicted in Fig. 5a, confirms the presence of Zr, P, W, and O elements in the 36.80$PW_{12}$/$ZrO_2$ material. The P 2p signal peak was observed at 134.0 eV, as shown in Fig. 5c. This peak shifted by 0.5 eV compared to that of the pure $PW_{12}$ sample, which appeared at 134.5 eV.[40] This shift suggests a change in the chemical environment of phosphorus upon its incorporation into the $ZrO_2$ matrix. Fig. 5d shows the peaks of the W 4f signal at 35.7 eV and 37.9 eV, indicating that tungsten mainly exists in the +6 oxidation state and may be the active site. Meanwhile, the Zr 3d signal peaks at 182.5 eV and 185.0 eV, as seen in Fig. 5e, are characteristic of zirconium in the +4 oxidation state, consistent with $Zr^{4+}$. Lastly, the O 1s signal peaks were observed at 530.3 eV, 531.4 eV, and 532.8 eV, as shown in Fig. 5b. These peaks correspond to oxygen in the $ZrO_2$ lattice, surface hydroxyl groups (–OH), and the oxygen atoms in the $PW_{12}$ moiety, respectively. Therefore, during the preparation of the 36.80$PW_{12}$/$ZrO_2$ composite material, the interaction between $PW_{12}$ and $ZrO_2$ was enhanced, which is conducive to stabilizing $W^{6+}$ and improving the catalytic performance.

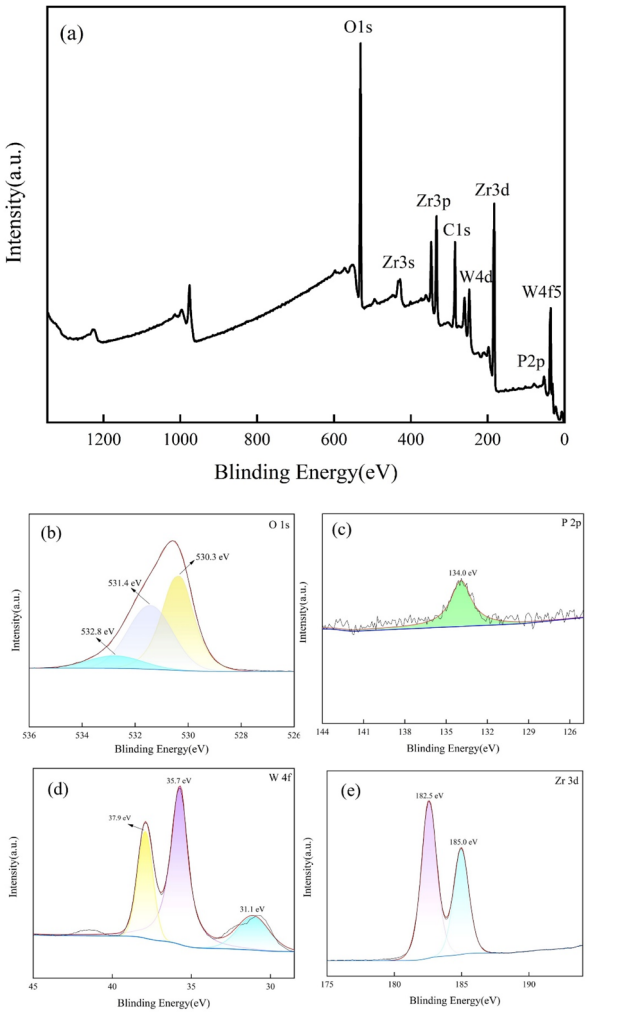


Fig. 5 XPS (a) survey spectrum and (b) O 1s, (c) P 2p, (d) W 4f, and (e) Zr 3d spectra.

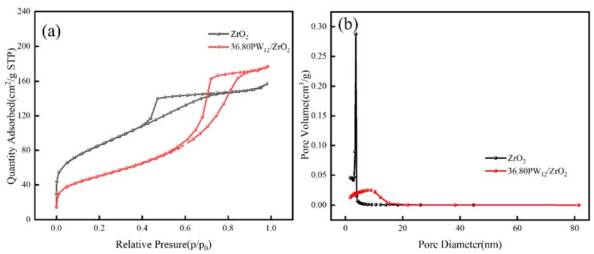


Fig. 4 (a) Nitrogen adsorption–desorption isotherms and (b) pore size distribution curves of $ZrO_2$ and 36.80$PW_{12}$/$ZrO_2$.

## Catalyst performance

In the process of oxidative desulfurization, $PW_{12}$ acts as the active component of the catalyst, and the loading of $PW_{12}$ has a significant impact on the performance of oxidative desulfurization. To evaluate the catalytic activity of the catalyst, Fig. 6 shows the influence of different $PW_{12}$ loadings on the performance of oxidative desulfurization. It can be seen from the figure that the desulfurization rate of DBT by $ZrO_2$ alone is only 75.30%. With the addition of $PW_{12}$, the desulfurization rate began to increase until the loading was 36.80 wt%, where the desulfurization performance was significantly improved, and the desulfurization rate reached 97.85% at 20 min. However, when it continued to increase, the desulfurization performance slightly decreased. The results show that during the experiment, introducing too few active components will lead to insufficient

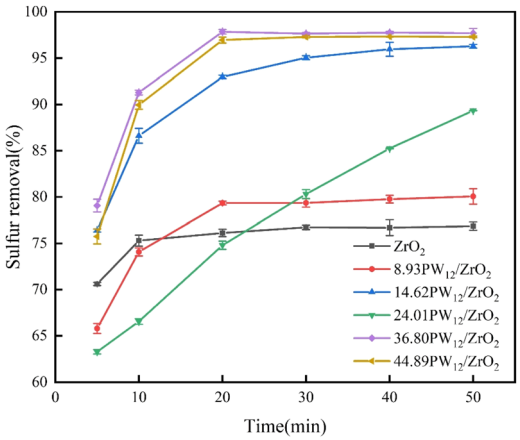


Fig. 6 Effect of different $PW_{12}$ loadings on oxidative desulfurization performance.

active sites in the catalyst, which cannot completely oxidize DBT, resulting in a low desulfurization rate. Alternatively, introducing too many active components will cause the aggregation of the active sites, and also reduce the catalytic performance. Therefore, the composite material with the best oxidation desulfurization performance was $36.80PW_{12}/ZrO_2$.

The reaction temperature is a pivotal factor that influences both the energy consumption and the duration of the ODS process. Fig. 7a illustrates the ODS performance of the $36.80PW_{12}/ZrO_2$ catalyst at various temperatures. It is evident that as the temperature increased, the catalytic activity for the oxidation of DBT by $36.80PW_{12}/ZrO_2$ also increased, as noted in reference.[41] However, at 70 °C, there was no further enhancement in ODS performance. This plateau is attributed to the accelerated decomposition of hydrogen peroxide at higher temperatures, which is detrimental to the catalysis, and thus 60 °C was identified as the optimal reaction temperature for this process. Furthermore, as shown in Fig. 8a, a linear relationship was obtained when ln $(C_0/C_t)$ was plotted against reaction time

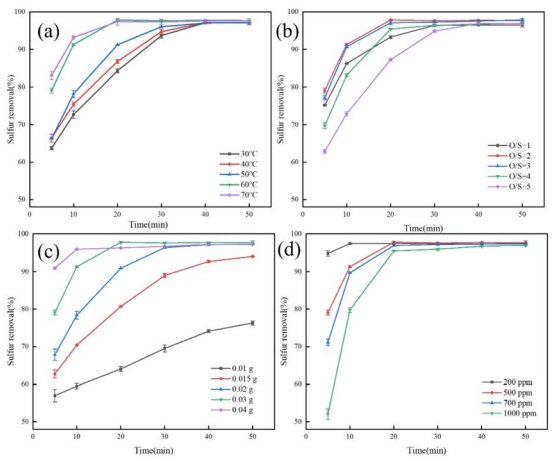


Fig. 7 Catalytic performance at (a) different reaction temperatures, (b) different amounts of $H_2O_2$, (c) different dosages of catalyst, and (d) different initial S-contents.

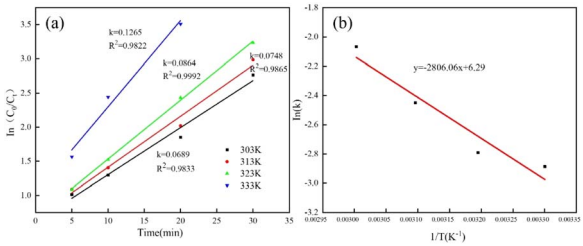


Fig. 8 (a) Pseudo-first-order kinetic curves and (b) Arrhenius plot.

at varying temperatures of 303, 313, 323, and 333 K. The apparent activation energy was calculated based on the reaction rate constant, $k$, measured at different temperatures. As shown in Fig. 8b, the apparent activation energy of oxidized DBT is 23.32 kJ mol$^{-1}$. The data in Fig. 8 can be fitted by the pseudo-first-order kinetic model using eqn (2) and (3), and the results are shown in Fig. 8.

$$k = Ae^{-E_a/RT} \quad (2)$$

$$\ln\frac{k_2}{k_1} = \frac{E_a}{R}\left(\frac{1}{T_1} - \frac{1}{T_2}\right) \quad (3)$$

The quantity of oxidant is another critical parameter that affects the efficacy of the ODS reaction. Based on the stoichiometry of the oxidative reaction from DBT to $DBTO_2$, the oxidation of 1 mole of DBT requires 2 moles of $H_2O_2$, according to reference.[42] Fig. 7b presents the experimental outcomes at different oxidant-to-sulfur molar ratios (O/S), conducted at 60 °C. The data indicate a marked improvement in desulfurization performance with an increase in the O/S molar ratio, reaching a peak of 97.85% within 20 min. However, when the O/S molar ratio surpassed 5, and then the desulfurization performance declined. This decrease is hypothesized to be due to the by-product water from $H_2O_2$ decomposition occupying the catalyst surface, thereby hindering the desulfurization process, as suggested in reference.[43] Thus, an O/S molar ratio of 3 was determined to be the most effective.

The catalyst dosage also plays a significant role in the catalytic performance. As depicted in Fig. 7c, the desulfurization performance improved from 75% to 97.85% as the catalyst dosage increased from 10 mg to 30 mg. This improvement is due to the increased availability of active sites. However, a further increment to 40 mg did not yield additional improvements. It appears that at higher catalyst dosages, some active sites may become occluded, leading to a reduction in the desulfurization performance. Therefore, a catalyst dosage of 30 mg was deemed optimal.

In practical applications, the sulfur content in oil depends on the quality of the oil, as indicated in reference.[44] Fig. 7d explores the ODS properties of model oils with varying sulfur concentrations. The desulfurization rate for the low-concentration oil (200 ppm) reached 97.49% within 10 min, while the high-concentration oil (1000 ppm) reached 96.80% within 40 min. The $36.80PW_{12}/ZrO_2$ catalyst demonstrated

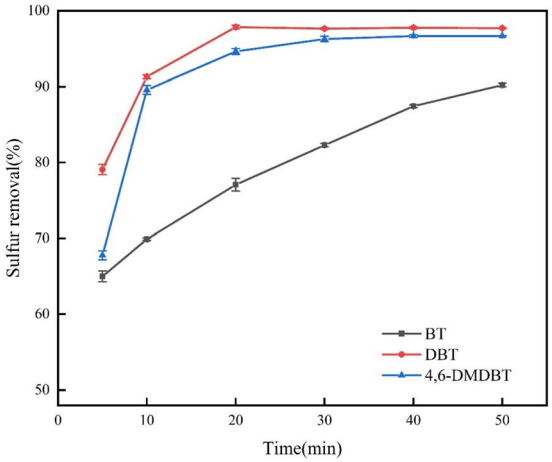


Fig. 9 Catalytic performance of different sulfur substrates.

exceptional catalytic activity and a robust desulfurization effect across a range of model oil concentrations.

As depicted in Fig. 9, a selection of aromatic sulfur compounds commonly found in fuel, including DBT, BT and 4,6-DMDBT, was examined for their desulfurization rates. The desulfurization rates for DBT, 4,6-DMDBT, and BT were recorded to be 97.85%, 96.68%, and 90.24%, respectively. The desulfurization efficiency followed the order of DBT > 4,6-DMDBT > BT, aligning with findings from other studies as reference.[45] In the oxidative desulfurization process, the desulfurization performance is predominantly influenced by the electron density surrounding the sulfur atoms. Compounds with higher electron density on their sulfur atoms exhibit a superior desulfurization performance.[46] BT having the lowest electron density on its sulfur atom exhibits the least reactivity among the three. DBT and 4,6-DMDBT possess comparable electron densities on their sulfur atoms, which accounts for their similar reactivity levels. However, the presence of two methyl groups in 4,6-DMDBT introduces steric hindrance, which diminishes the interaction between acetonitrile and $H_2O_2$. This reduced interaction adversely affects the desulfurization process, leading to a lower desulfurization performance for 4,6-DMDBT in comparison to DBT. This observation underscores the importance of molecular structure in the catalytic desulfurization process. Thus, to fully understand the excellent ODS activity of heteropoly acids, the oxidative desulfurization performance of several representative catalysts for different sulfides is summarized in Table S3.†

The recycling stability of the catalyst is a critical aspect of this study. After each use, the catalyst was isolated from the reaction mixture and subjected to drying in an oven at 60 °C for a duration of 12 h. Subsequently, fresh model oil was introduced for subsequent ODS reactions. As illustrated in Fig. 10a, there was a slight reduction in the desulfurization performance, but it remained commendable at 90%. As shown in Fig. 10b, the catalytic performance was almost completed stopped when the catalyst was filtered from the ODS system at 5 min, indicating its good reusability and stability. The structural integrity of the

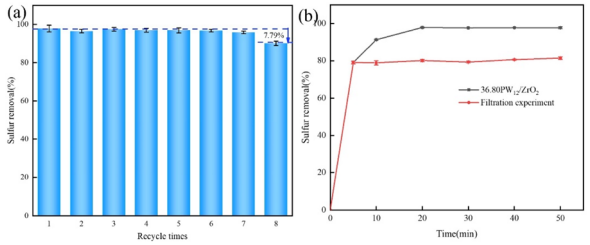


Fig. 10 Recycling performance of the 36.80$PW_{12}/ZrO_2$ catalyst. (b) Sulfur removal of DBT catalyzed by the catalyst.

catalyst was further assessed using Fourier-transform infrared spectroscopy (FT-IR). Fig. S2† presents the FT-IR spectra, which reveal that the spectrum of the recovered catalyst closely matches that of the fresh catalyst. This consistency suggests that the structure of the catalyst was preserved, confirming its robust recyclability and stability. These findings are encouraging for the practical application of the catalyst, given that they demonstrate its potential for sustained performance over extended periods of use.[47]

To identify the free radicals produced in oxidative desulphurization (ODS) reactions, we strategically used dimethyl sulfoxide (DMSO), benzoquinone (BQ), and silver nitrate ($AgNO_3$) as scavengers targeting hydroxyl ($\cdot OH$), superoxide ($\cdot O^{2-}$), and electron ($e^-$) radicals, respectively. As shown in Fig. 10a, the activity of ODS at 36.80$PW_{12}/ZrO_2$ was slightly affected. In contrast, the activity of $ZrO_2$ was completely suppressed after the addition of DMSO (Fig. S3a and b†). The primary active material of 36.80$PW_{12}/ZrO_2$ during oxidative desulphurization is not free radicals, although the presence of free radicals was shown in electron EPR, possibly due to the contribution of a portion of the site of the unloaded $PW_{12}$ (Fig. 11b). Thus, it can be inferred that the synergistic effect changes the reaction pathway.[48,49]

To delve into the oxidative desulfurization process and track the transformation of dibenzothiophene (DBT), gas chromatography-mass spectrometry (GC-MS) was employed to scrutinize both the oil phase and the extraction phase. Fig. 12 displays a pronounced peak attributed to the presence of DBT ($m/z = 184.1$) in the model oil. As the reaction proceeded, the intensity of this peak diminished progressively, signifying the gradual consumption of DBT. Post-reaction, the chromatogram revealed the absence of DBT, indicating near-complete removal. Concomitantly, the GC spectrum of the extraction phase

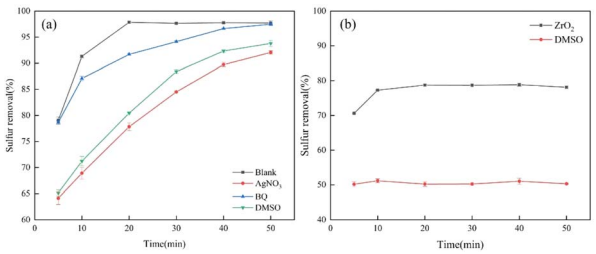


Fig. 11 (a and b) Radical quenching experiments over 36.80$PW_{12}/ZrO_2$ and $ZrO_2$ in ODS.

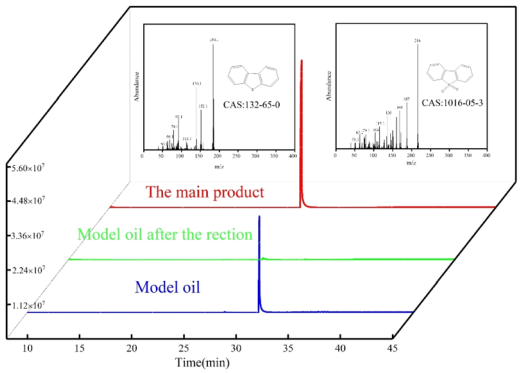


Fig. 12 GC-MS spectra of the oil phase and MeCN phase.

unveiled an emergent peak corresponding to the mass-to-charge ratio ($m/z$ = 216) of the oxidized product, $DBTO_2$. This observation confirms the conversion of DBT into its corresponding sulfone, $DBTO_2$, which is subsequently adsorbed on the catalyst surface. The detection of $DBTO_2$ in the extraction phase underscores the efficacy of the oxidative desulfurization process in transforming DBT into a more polar and easily removable species.

Based on the analytical findings, a plausible reaction mechanism for the ODS process was deduced and is illustrated in Scheme 2. The mechanism unfolds in a series of orchestrated steps.

Initially, DBT present in the model oil is extracted into the acetonitrile phase, where it is solubilized and prepared for the subsequent oxidative attack. Subsequently, the tungsten(VI) center in the catalyst (denoted W=O) is oxidized, initiating the catalytic cycle, denoted as W=O, to form reactive tungsten(VI) oxide species, characterized as a $WO_2$ ternary ring structure. Concurrently, DBT is oxidatively transformed into its corresponding sulfoxide (DBTO). This step marks the beginning of the sulfur heteroatom conversion. Then, the $WO_2$ species then regenerated to its original W=O state, ready to engage in another catalytic cycle, while DBTO is further oxidized to its sulfone derivative, $DBTO_2$. The final step involves the complete oxidation of $DBTO_2$, leading to the detachment of the sulfur atom from the hydrocarbon framework and its subsequent removal from the oil phase.

Through this cascade of reactions, the ODS process reaches completion, culminating in the production of sulfur-free oil. This mechanism not only elucidates the role of each component in the reaction mixture but also highlights the regenerative nature of the catalyst, ensuring a sustainable and efficient desulfurization process.

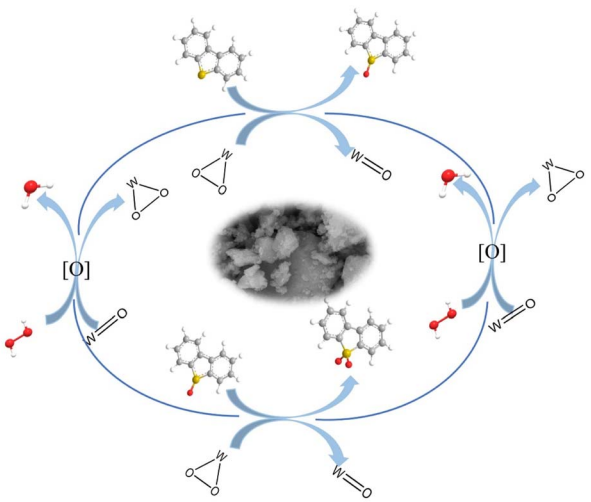


Scheme 2 Schematic of the possible reaction mechanism of the catalyst.

## Conclusion

In this paper, phosphotungstic acid was successfully loaded on zirconia *via* the sol–gel method, and an extraction-catalytic oxidation system was formed with acetonitrile and hydrogen peroxide. Compared with other literature methods,[44] this catalyst not only has good oxidation desulfurization performance for DBT, but also for other sulfides. This catalyst is reused 8 times, and its composition and performance do not change significantly. Compared with the non-recyclable catalysts reported in the literature,[50] it has significant economic advantages. The catalysis mechanism of this experiment was confirmed by the quenching experiment of hyperradical and ESR analysis. This study provides the possibility and reference value for the deep desulfurization of fuel oil. In future research, it is necessary to employ real fuel as the object and achieve industrial application to further improve the efficiency and economy of oxidation desulfurization technology and make greater contributions to environmental protection and sustainable energy utilization.

## Data availability

Data supporting this article have been submitted as part of ESI.†

## Author contributions

Rui Liang: conceptualization, investigation, methodology, formal analysis, and writing – original draft. Yu Hu: formal analysis and methodology. YuFang Ye: investigation and visualization. Qing Wang: conceptualization, resources, funding acquisition, supervision, project administration, and writing – review & editing.

## Conflicts of interest

There are no conflicts to declare.

## Acknowledgements

Financial support from the Xinjiang Uygur Autonomous Region Natural Science Foundation General Project (2019D01A72) is acknowledged.

## References


1 M. R. H. Moghaddam and M. N. Shahrak, *Chem. Commun.*, 2024, **165**, 112489.
2 K. Stawicka, J. Gajewska, M. Ziolek and M. Trejda, *Molecules*, 2025, **30**, 551.
3 I. Ahmed and S. H. Jhung, *Fuel*, 2025, **393**, 135043.
4 Z. Zaidi, Y. Gupta, S. Gayatri and A. Singh, *Inorg. Chem. Commun.*, 2023, **154**, 110964.
5 R. Liu, S. Dou, M. Yu and R. Wang, *Egypt. J. Pet.*, 2018, **27**, 715–730.
6 Y. Liu, J. Xue, X. Zhou and Y. Cui, *R. Soc. Open Sci.*, 2021, **8**, 201736.
7 B. Wang, L. Kang and M. Zhu, *Nanomaterials*, 2021, **11**, 2369.
8 H. Zhang, T. Wang, B. Wang, W. Guo, X. Miao and X. Liang, *RSC Adv.*, 2023, **13**, 35689.
9 X. Qiu, B. Wang, R. Wang and I. V. Kozhevnikov, *Materials*, 2024, **17**, 1803.
10 C. Shu, M. Zhao, H. Chen, P. Stiernet, N. Hedin and J. Yuan, *React. Chem. Eng.*, 2023, **8**, 3124.
11 L. Xu, Q. Tong and B. Wang, *RSC Adv.*, 2024, **49**, 36622–36632.
12 H. Zhang, G.-R. Qian and H. Liu, *Microporous Mesoporous Mater.*, 2022, **346**, 112296.
13 Y. N. Prajapati and N. Verma, *Fuel*, 2017, **189**, 186–194.
14 C. Yang, B. Wu, Z. Liu, G. Miao, Q. Xia, Z. Li, M. J. Janik and G. Li, *Chin. J. Chem. Eng.*, 2022, **42**, 25–34.
15 M. Zhang, X. Yi, J. Deng, F. Kang, Y. Li and J. Qiang, *Fuel*, 2025, **397**, 135398.
16 G. Yu, D. Jin, X. Li, F. Zhang, S. Tian, Y. Qu, Z. Zhou and Z. Ren, *Front. Chem. Sci. Eng.*, 2022, **16**, 1735–1742.
17 R. Wu, C. Mao, Y. Zhou, H. Sun and J. Xu, *Appl. Organomet. Chem.*, 2025, **39**, 70147.
18 G. Lei, W. Zhao, L. Shen, S. Liang, C. Au and L. Jiang, *Appl. Catal., B*, 2020, **267**, 118663.
19 J. Shen, G. Lv, J. Deng, S. Su, F. Wang, S. Xu, L. Oussama and Z. Liu, *Separation Purif. Technol.*, 2025, **364**, 132299.
20 M. Yan, J. Huang, S. Zhao, X. Dong, Y. Gao and J. Zhao, *Chem. Eng. Sci.*, 2024, **298**, 120350.
21 J. Guo, L. Ch, H. Yang, Z. Huang, M. Yang and Ge. Wang, *Chem. Eng. J.*, 2023, **451**, 138595.
22 X. An, W. Jiang, L. Zhu, L. Xu, J. She, J. He, W. Zhu and H. Li, *Appl. Catal., B*, 2023, **333**, 122779.
23 Z. Qi, H. Li, J. Chen, C. Ye and T. Qiu, *Fuel*, 2022, **322**, 124231.
24 S. Vedachalam, P. E. Boahene and A. K. Dalai, *Energy Fuels*, 2020, **34**, 15299–15312.
25 J. Xiong, H. Huang, M. Zhang, P. Song, H. Li and J. Di, *Fuel*, 2024, **365**, 131168.
26 J. Wang, G. Ye, H. Wang, H. Chen, H. Chu, J. Wei, D. Wang and Y. Li, *Angew. Chem., Int. Ed.*, 2021, **60**, 20318–20324.
27 G. Ye, H. Wang, X. Zeng, L. Wang and J. Wang, *Appl. Catal., B*, 2021, **299**, 120659.
28 L. Chen, J. T. Ren and Z. Y. Yuan, *Appl. Catal., B*, 2022, **305**, 121044.
29 M. A. Rezvani, Y. Khoshkbari, N. Khalafi and S. A. Mirsadri, *Inorg. Chem. Commun.*, 2025, **177**, 114306.
30 Z. Li, L. Huang, X. Yu, K. Huang, W. Cui and H. Zhang, *Energy Fuels*, 2024, **38**, 13218–13227.
31 P. Wang, M. Gan, P. Deng and Y. Xu, *Chem. Commun.*, 2021, **133**, 108922.
32 J. Alcañiz-Monge, E. B. Bakkali, G. Trautwein and R. Santiago, *Appl. Catal., B*, 2018, **224**, 194–203.
33 M. Wu, X. Zhang, X. Su, X. Li, X. Zheng, X. Guan and P. Liu, *Catal. Commun.*, 2016, **85**, 66–69.
34 J. Yuan, J. Xiong, J. Wang, W. Ding, L. Yang, M. Zhang, W. Zhu, H. Li and J. Porous, *Mater*, 2016, **23**, 823–831.
35 S. Nasiri, M. Rabiei, A. Palevicius, G. Janusas, A. Vilkauskas, V. Nutalapati and A. Monshi, *Nano Trends*, 2023, **3**, 100015.
36 L. Zhang, S. Wu, Y. Liu, F. Wang, X. Han and H. Shan, *Appl. Organomet. Chem.*, 2016, **30**, 684–690.
37 S. Mallick and K. M. Parida, *Catal. Commun.*, 2007, 889–893.
38 Y. Liu, P. Zou, Z. Xie, W. Jiao and R. Wang, *Fuel*, 2024, **375**, 132585.
39 P. Wu, Y. Wu, L. Chen, J. He, M. Hua, F. Zhu, X. Chu, J. Xiong, M. He, W. Zhu and H. Li, *Chem. Eng. J.*, 2020, **280**, 122526.
40 M. S. Akhtar, K. K. Cheralathan, J.-M. Chun and O.-B. Yang, *Electrochim. Acta*, 2008, **53**, 6623–6628.
41 S. Gao, Y. Yu, H. Y. Li, R. J. Zhang, C. J. Zou, S. Y. Yao and L. X. Chen, *J. Solid State Chem.*, 2024, **332**, 124587.
42 Y. Lu, C. Yue, B. Liu, M. Zhang, Y. Li, W. Yang, Y. Lin, Y. Pan, D. Sun and Y. Liu, *Microporous Mesoporous Mater.*, 2021, **311**, 110694.
43 S. Wang, P. Li, L. Hao, C. Deng, W. Ren and H. Lü, *Chem. Eng. Technol.*, 2017, **40**, 555–560.
44 X. Zhou, J. Jiao and W. Jiao, *Dalton Trans.*, 2023, **52**, 17524.
45 H. Xu, D. Zhang, F. Wu and R. Cao, *Fuel*, 2017, **208**, 508–513.
46 B. N. Bhadra and S. H. Jhung, *Appl. Catal., B*, 2019, **259**, 118021.
47 G. Ye, L. L. Hu, Y. L. Gu, C. Lancelot, A. Rivers, C. Lamonier, N. Nuns, M. Marinova, W. Xu and Y. Y. Sun, *J. Mater. Chem. A*, 2020, **8**, 19396.
48 Q. Huo, G. Liu, H. Sun, Y. Fu, Y. Ning, B. Zhang, Z. Zhang, X. Zhang, J. Gao, J. Miao, X. Zhang and S. Liu, *Chem. Eng. J.*, 2021, **422**, 130036.
49 G. Ye, M. Zheng, Q. L. Zhang, J. Zhou, L. Wu and J. Wang, *Small*, 2023, **19**, 2301035.
50 L. E. P. Santiago, M. G. Silva and E. V. Sobrinho, *Ind. Eng. Chem. Res.*, 2023, **62**(47), 20393–20403.